Electronic Supplementary Information

Upcycling of plastic waste to atomic nickel sites decorated carbon for efficient electrochemical CO_2 conversion

Lan-Hui Feng, Zhi-Hui Lv, Yi-Jie Kong, Xin-Ming Hu*

Environment Research Institute, Shandong University, Qingdao 266237 (China)

*E-mail: huxm@sdu.edu.cn

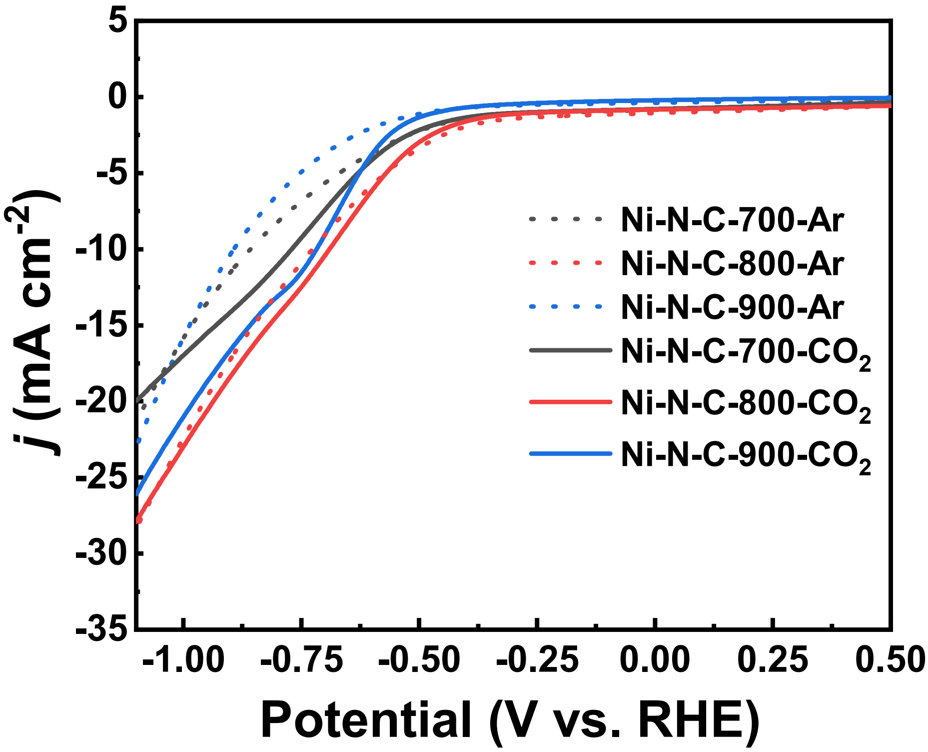

Fig. S1 Linear sweep voltammograms of Ni-N-C-*T* (*T* = 700, 800, and 900 °C) recorded at a sweep rate $\boldsymbol{v}$ = 10 mV s^{-1} in Ar- or CO_2-saturated 0.5 M $KHCO_3$ solution.

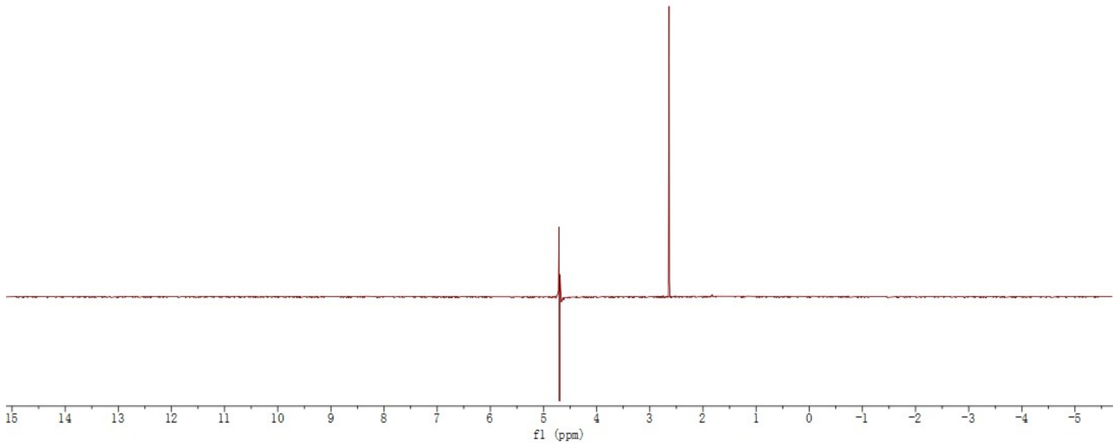

Fig. S2 ^{1}H NMR spectrum of the cathodic electrolyte after 20 min electrolysis of CO_2 at –0.87 V vs RHE in 0.5 M $KHCO_3$ using Ni-N-C-800. The two peaks observed are attributed to the H coming from water and DMSO that is added as the internal reference.

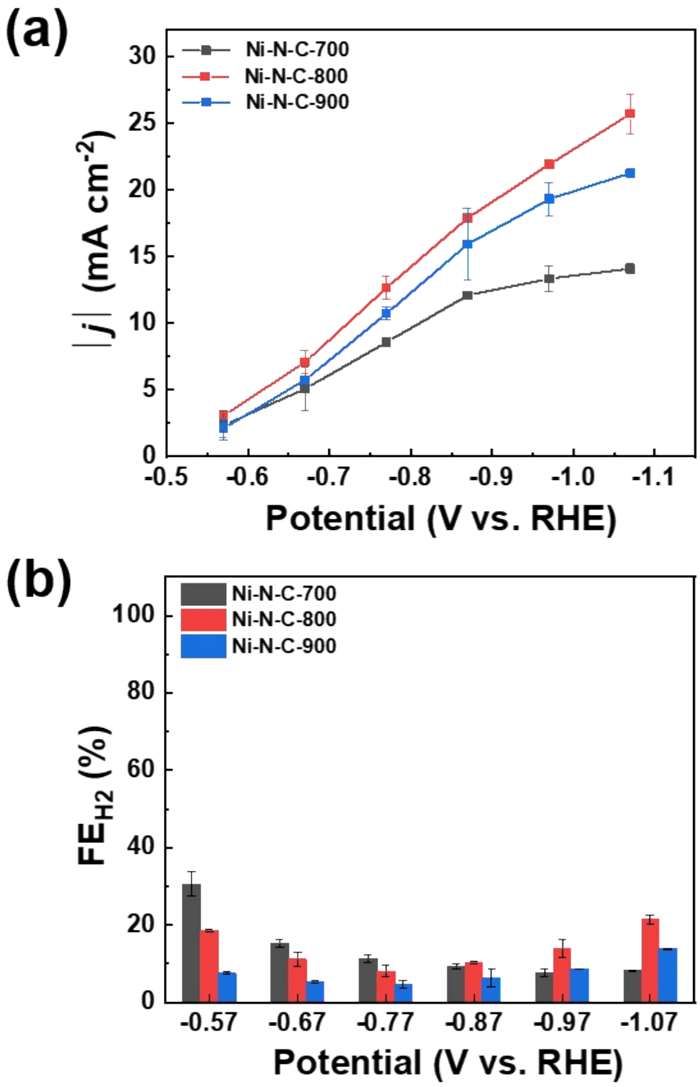

Fig. S3 (a) |*j*| and (b) FE_{H2} measured after 20 min electrolysis at various potentials for Ni-N-C-*T* (*T* = 700, 800, and 900 °C).

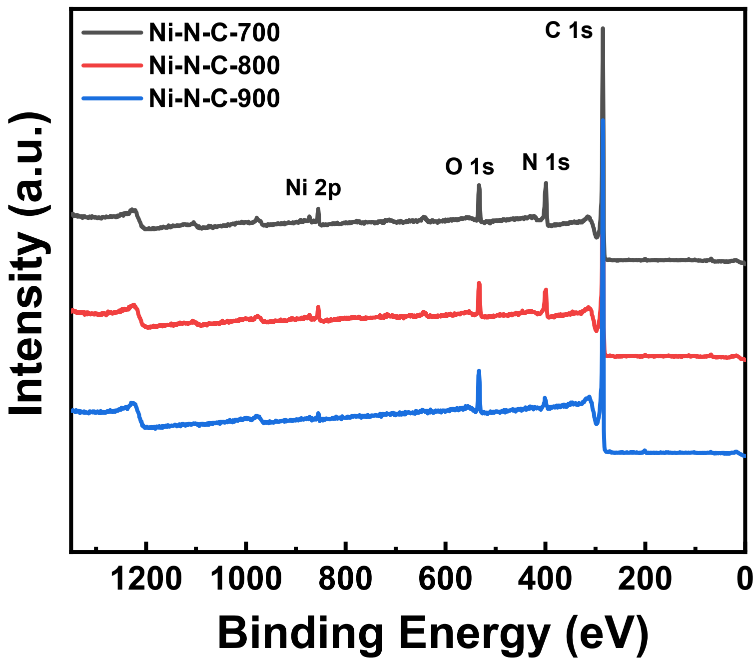

Fig. S4 XPS survey spectra of Ni-N-C-*T* (*T* = 700, 800, and 900 °C).

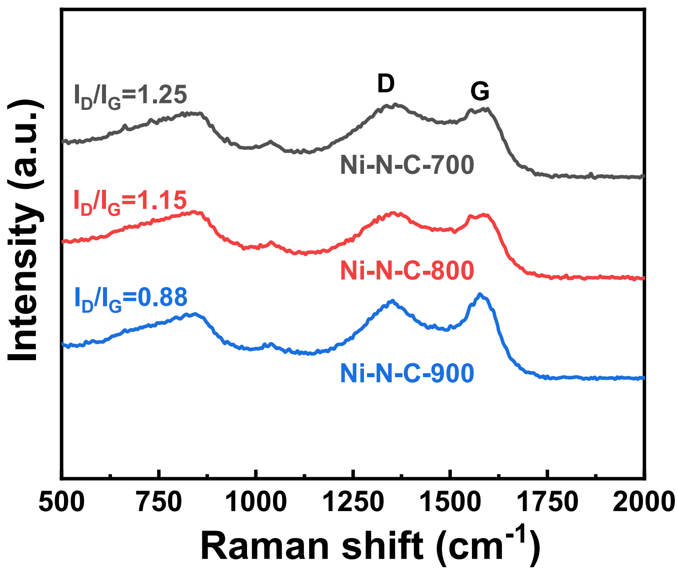

Fig. S5 Raman spectra of Ni-N-C-*T* (*T* = 700, 800, and 900 °C).

The small peak around 1050 cm^{-1} comes from the glass slide, while the broad peak around 850 cm^{-1} may come from the equipment itself.

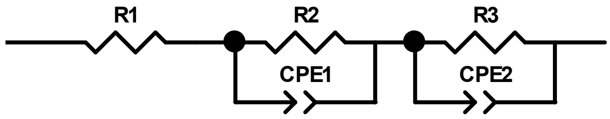

Fig. S6 Equivalent circuit model (R_1: solution resistance, R_2: ohmic resistance, R_3: charge transfer resistance).

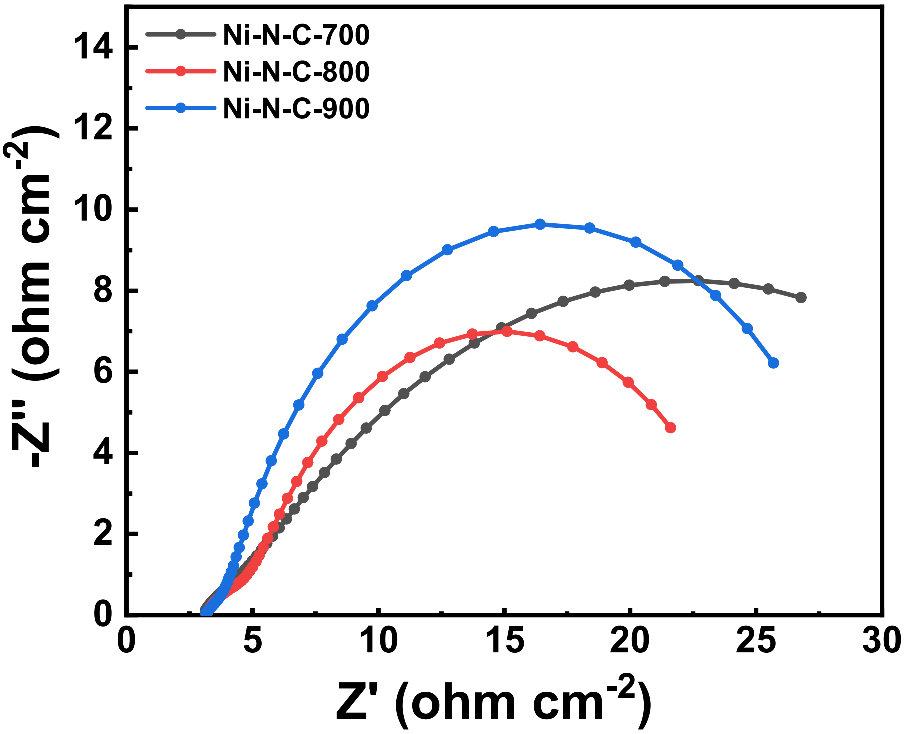

Fig. S7 Nyquist plots of Ni-N-C-*T* (*T* = 700, 800, and 900 °C).

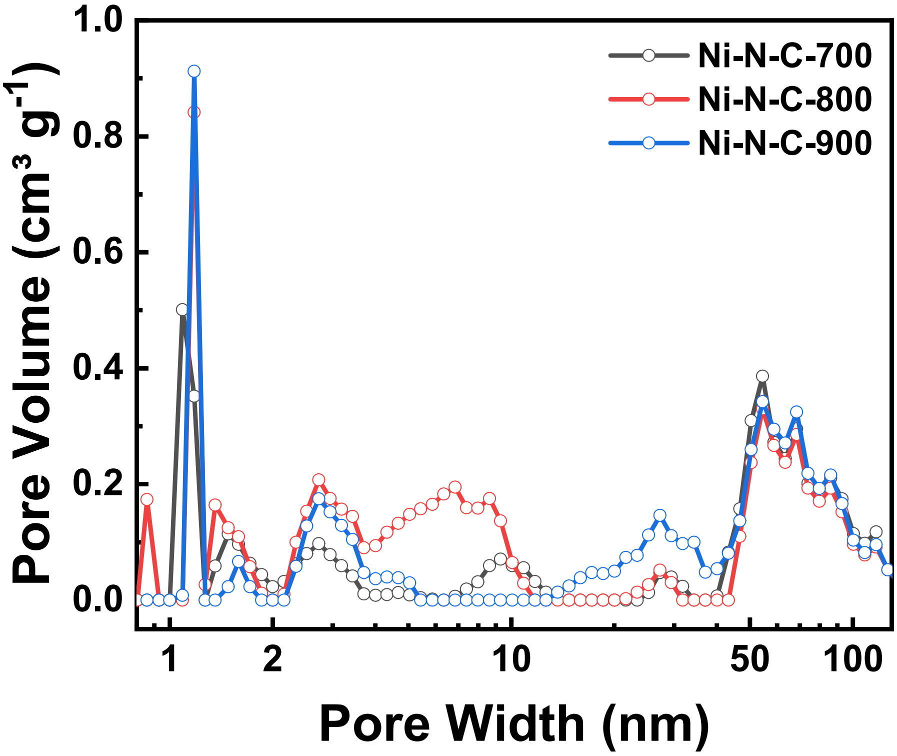

Fig. S8 (a) N_2 adsorption-desorption isotherms and (b) pore size distributions of Ni-N-C-*T* (*T* = 700, 800, and 900 °C).

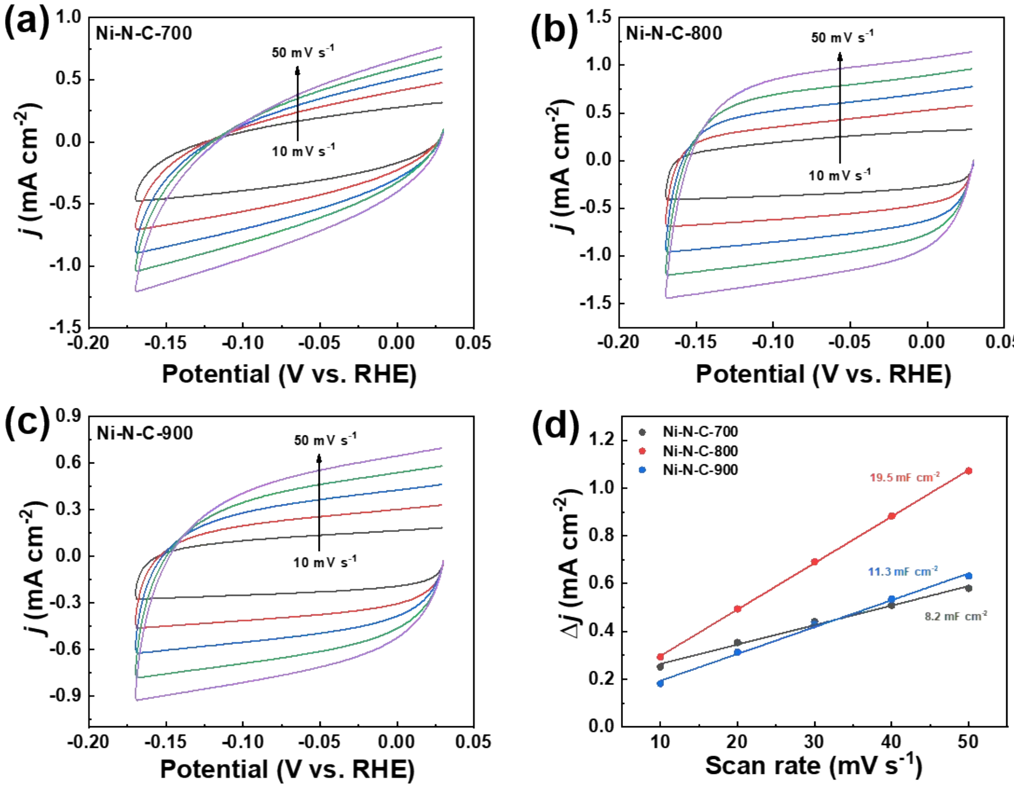

Fig. S9 (a–c) Cyclic voltammograms recorded at Ni-N-C-*T* (*T* = 700, 800, and 900 °C) between 0.03 and –0.17 V vs RHE using $\boldsymbol{v}$ = 10, 20, 30, 40 and 50 mV s^{-1} in CO_2-saturated 0.5 M $KHCO_3$; (d) the plot of double layer current density, Δ*j*, obtained at –0.07 V vs RHE from voltammograms (a–c) against the scan rate.

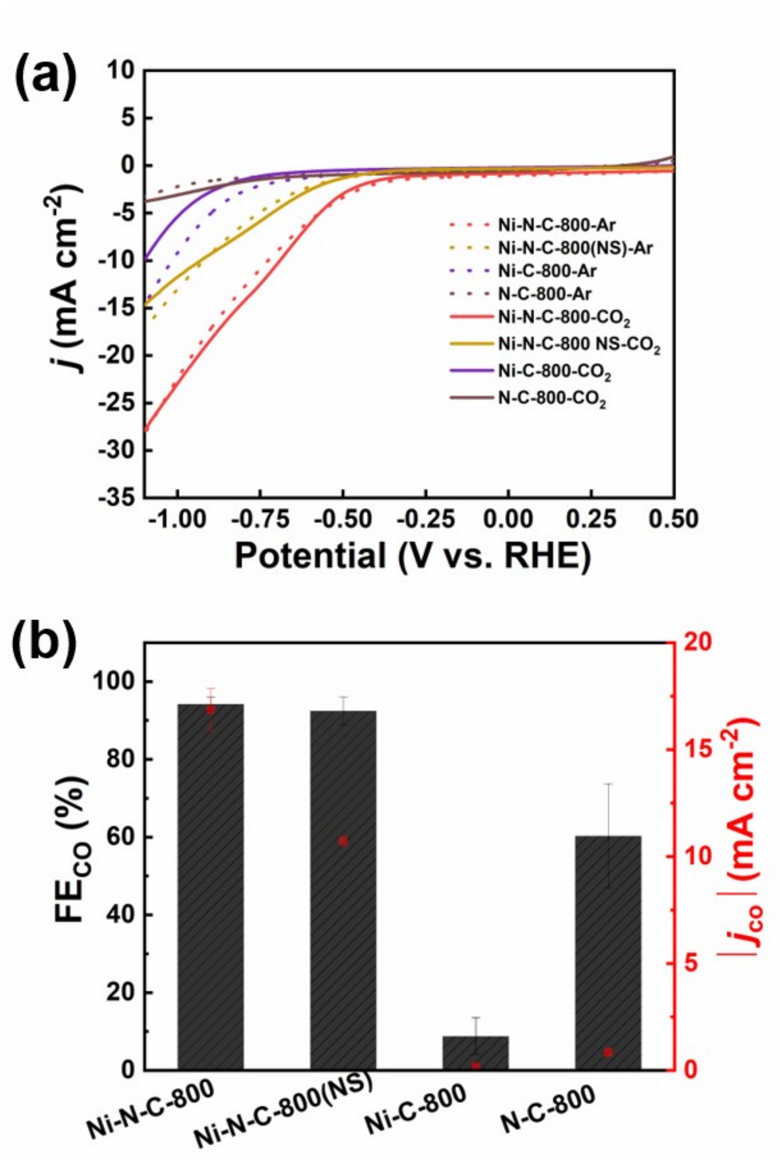

Fig. S10 (a) Linear sweep voltammograms of Ni-N-C-800, Ni-N-C-800(NS), Ni-C-800, and N-C-800 recorded at a sweep rate $\boldsymbol{v}$ = 10 mV s^{-1} in Ar- or CO_2-saturated 0.5 M $KHCO_3$ solution, (b) FE_{CO} and $|j_{co}|$ measured after 20 min electrolysis at –0.87 V vs RHE for Ni-N-C-800, Ni-N-C-800(NS), Ni-C-800, and N-C-800.

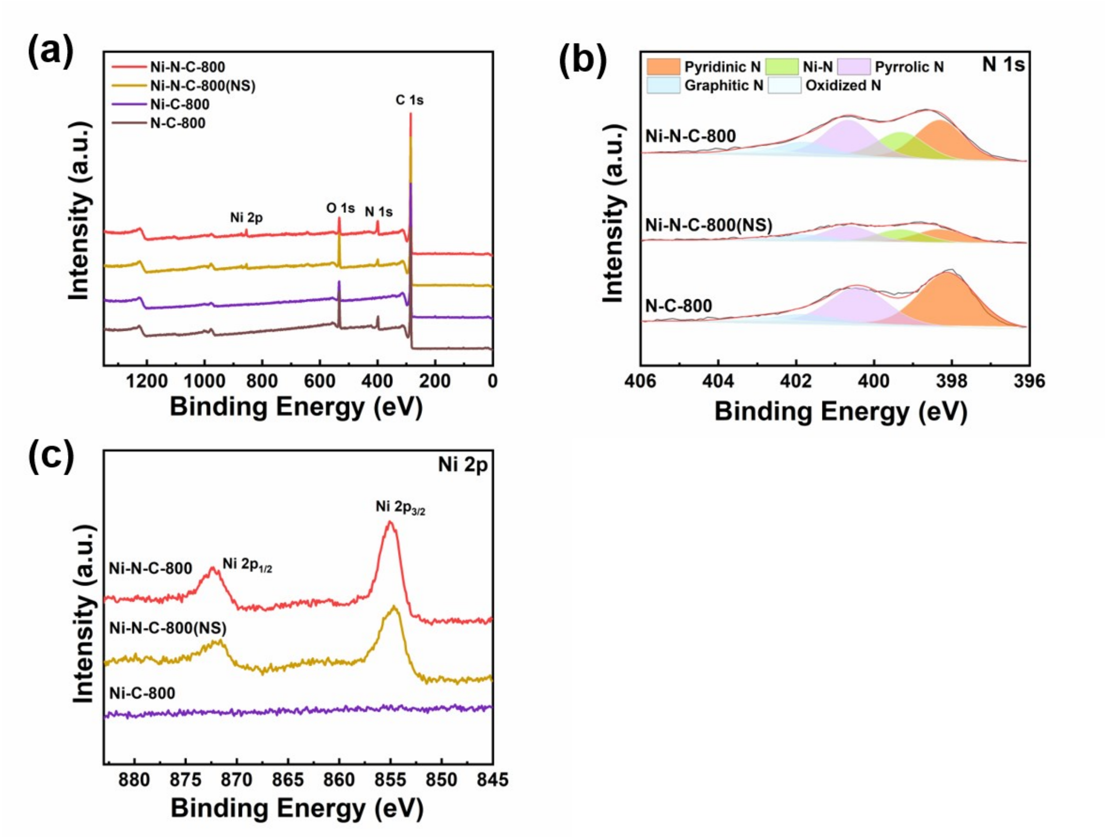

Fig. S11 XPS (a) survey, (b) N 1s, and (c) Ni 2p spectra of the materials.

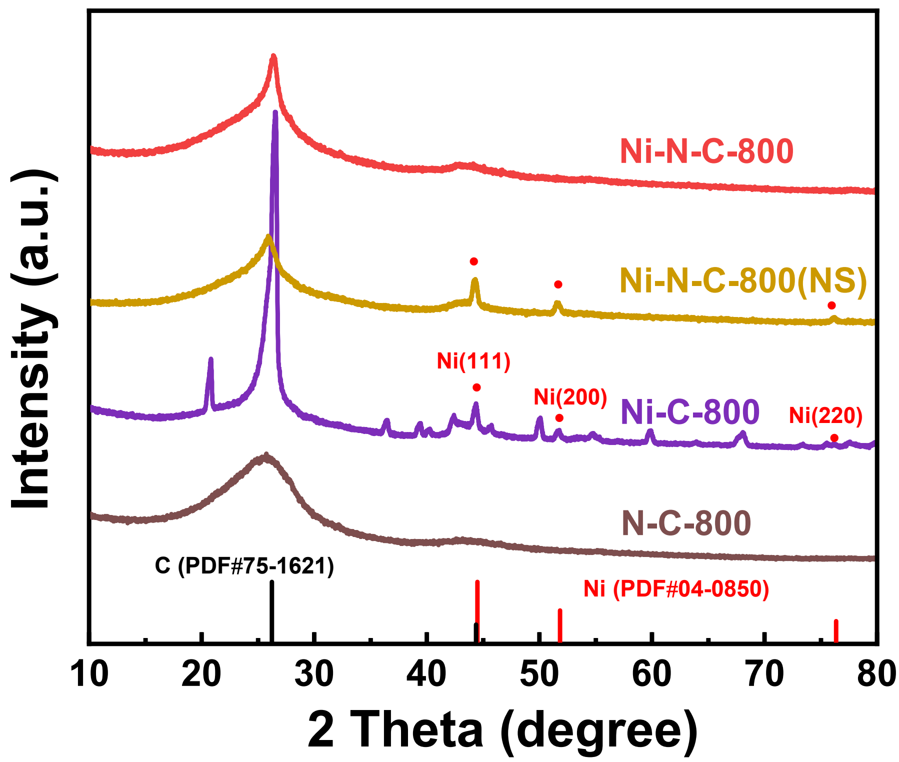

Fig. S12 XRD of Ni-N-C-800, Ni-N-C-800(NS), Ni-C-800, and N-C-800.

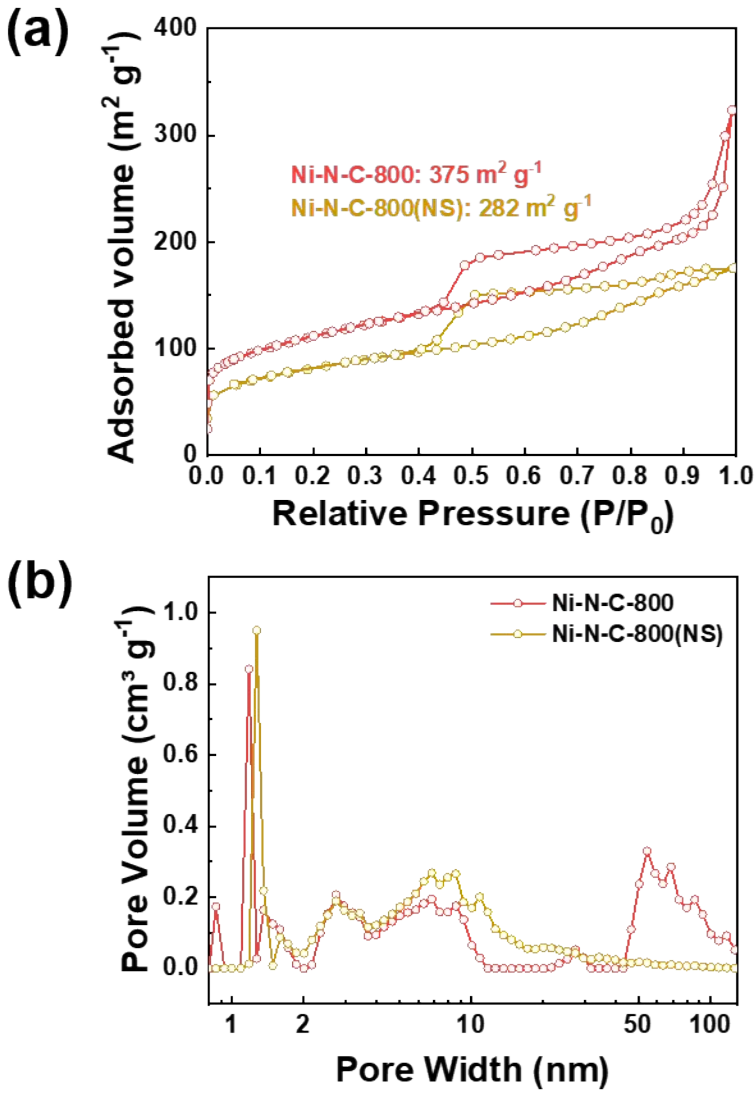

Fig. S13 (a) N_2 adsorption-desorption isotherms and (b) pore size distributions of Ni-N-C-800 and Ni-N-C-800(NS).

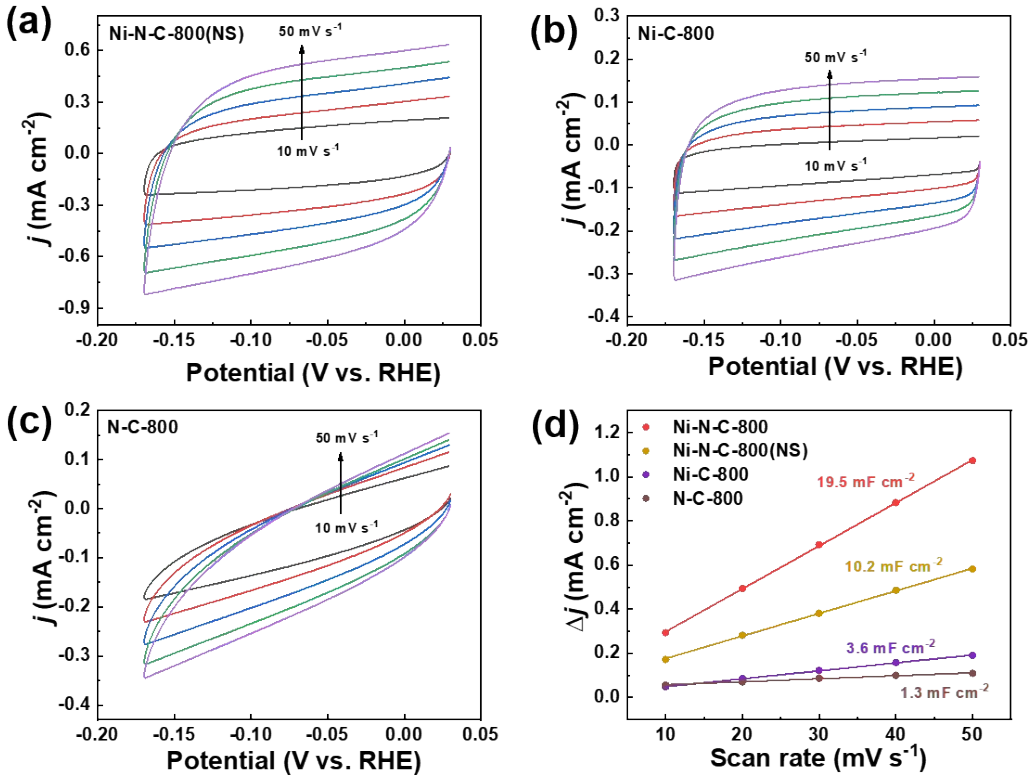

Fig. S14 (a−c) Cyclic voltammograms recorded at Ni-N-C-800(NS), Ni-C-800, and N-C-800 between 0.03 and –0.17 V vs RHE using ν = 10, 20, 30, 40, and 50 mV s^{-1} in CO_2-saturated 0.5 M $KHCO_3$; (d) the plot of double layer current density, Δ*j*, obtained at –0.07 V vs RHE from voltammograms (a−c) against the scan rate.

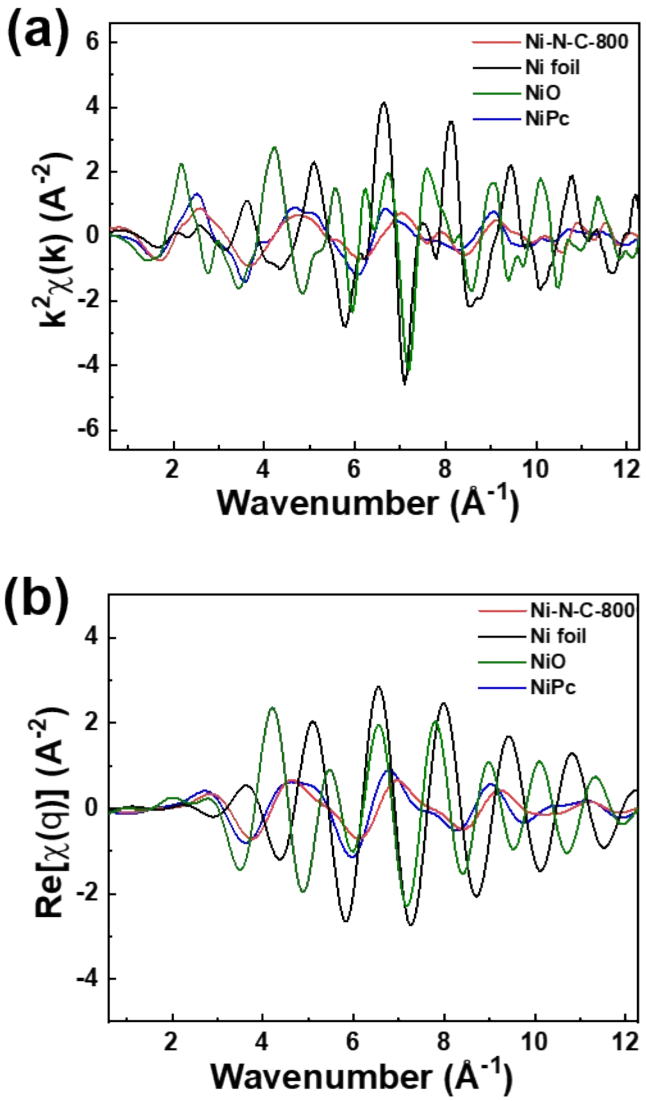

Fig. S15 (a) k^2-weighted *k*-space and (b) *q*-space spectra of Ni-N-C-800, Ni foil, NiO, and NiPc.

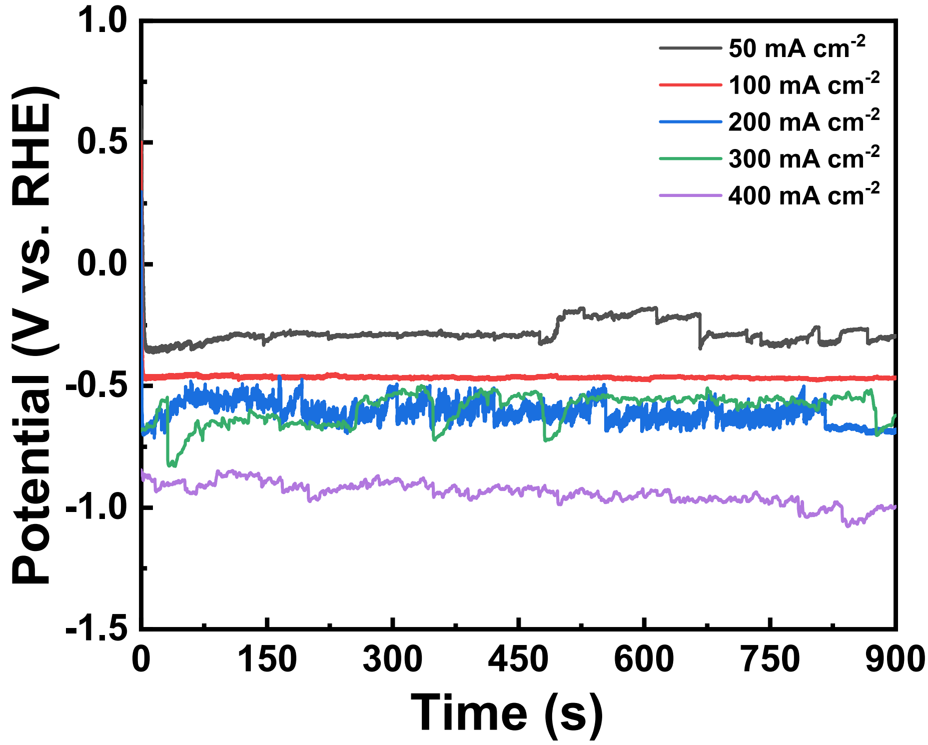

Fig. S16 Working potential of Ni-N-C-800 recorded for 900 s electrolysis at different current density.

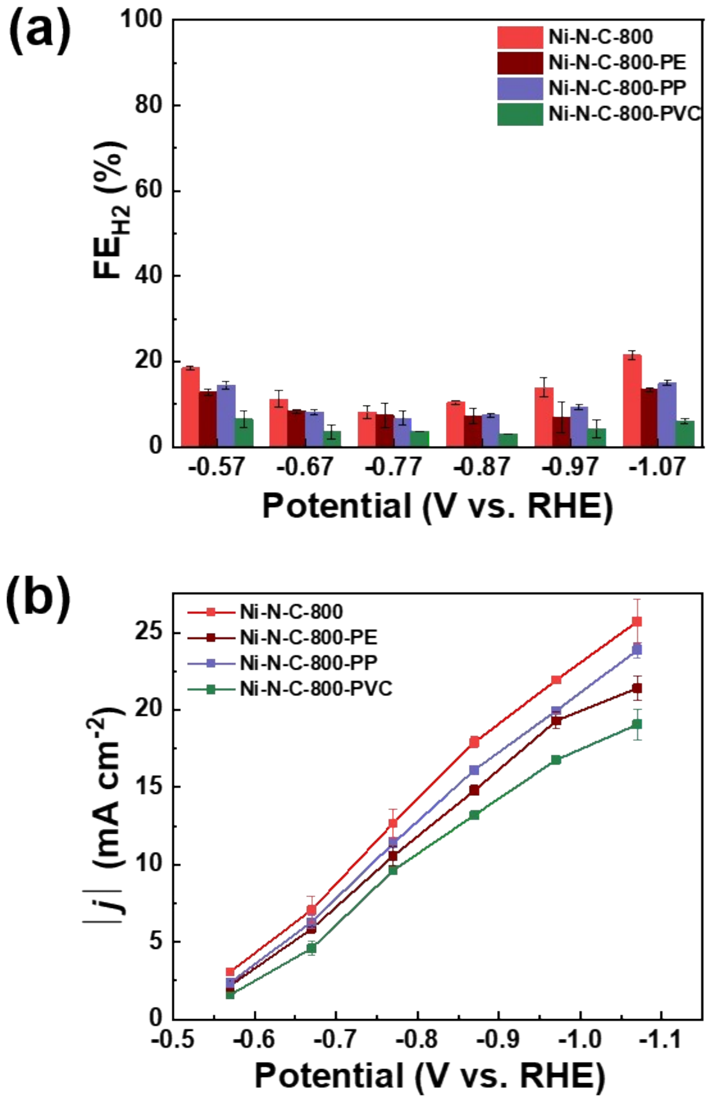

Fig. S17 (a) FE$_{H2}$ and (b) $|j|$ measured after 20 min electrolysis at varying potentials on Ni-N-C-800, Ni-N-C-800-PE, Ni-N-C-800-PP, and Ni-N-C-800-PVC.

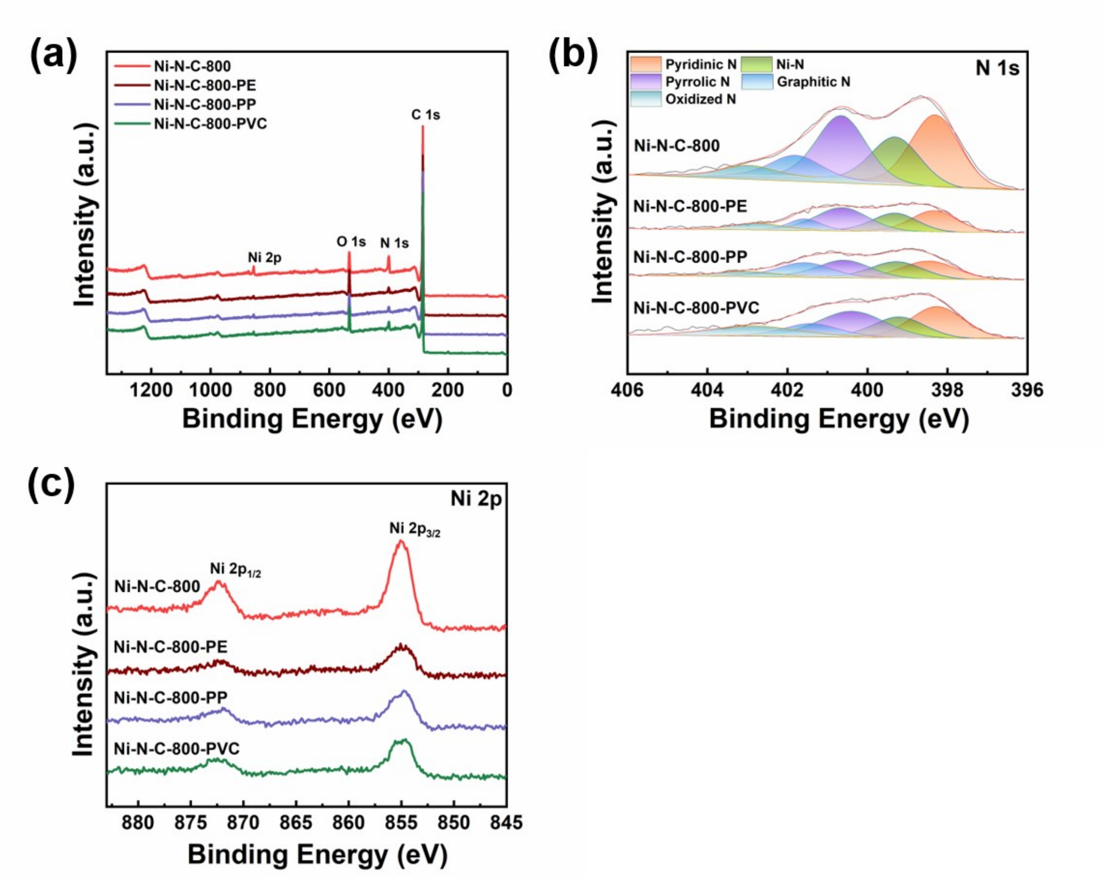

Fig. S18 (a) XPS survey spectra, (b) N 1s spectra and (c) Ni 2p spectra of Ni-N-C-800, Ni-N-C-800-PE, Ni-N-C-800-PP, and Ni-N-C-800-PVC.

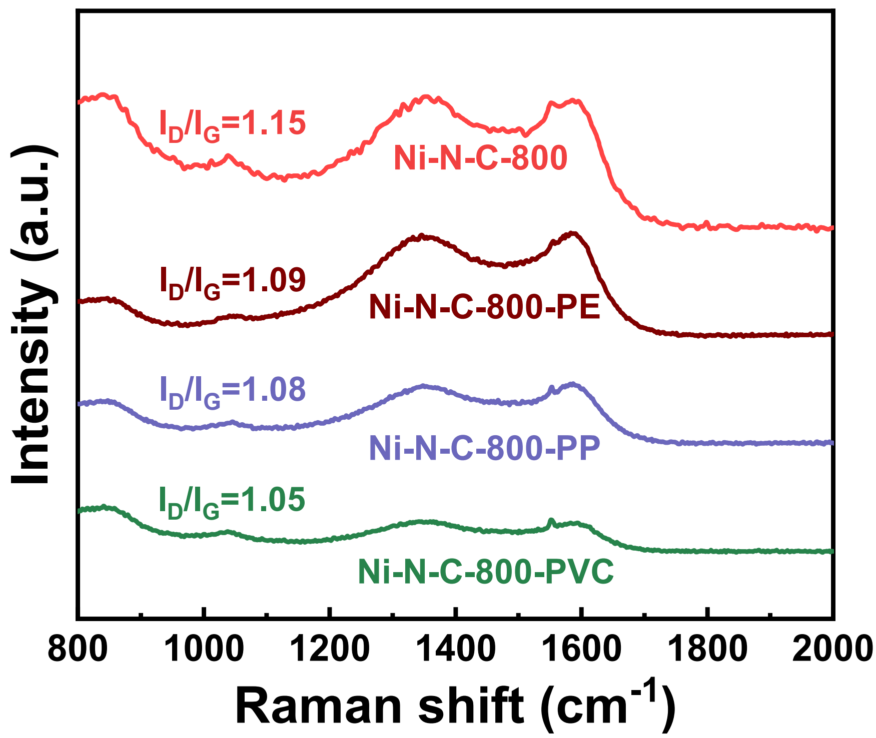

Fig. S19 Raman spectra of Ni-N-C-800, Ni-N-C-800-PE, Ni-N-C-800-PP, and Ni-N-C-800-PVC.

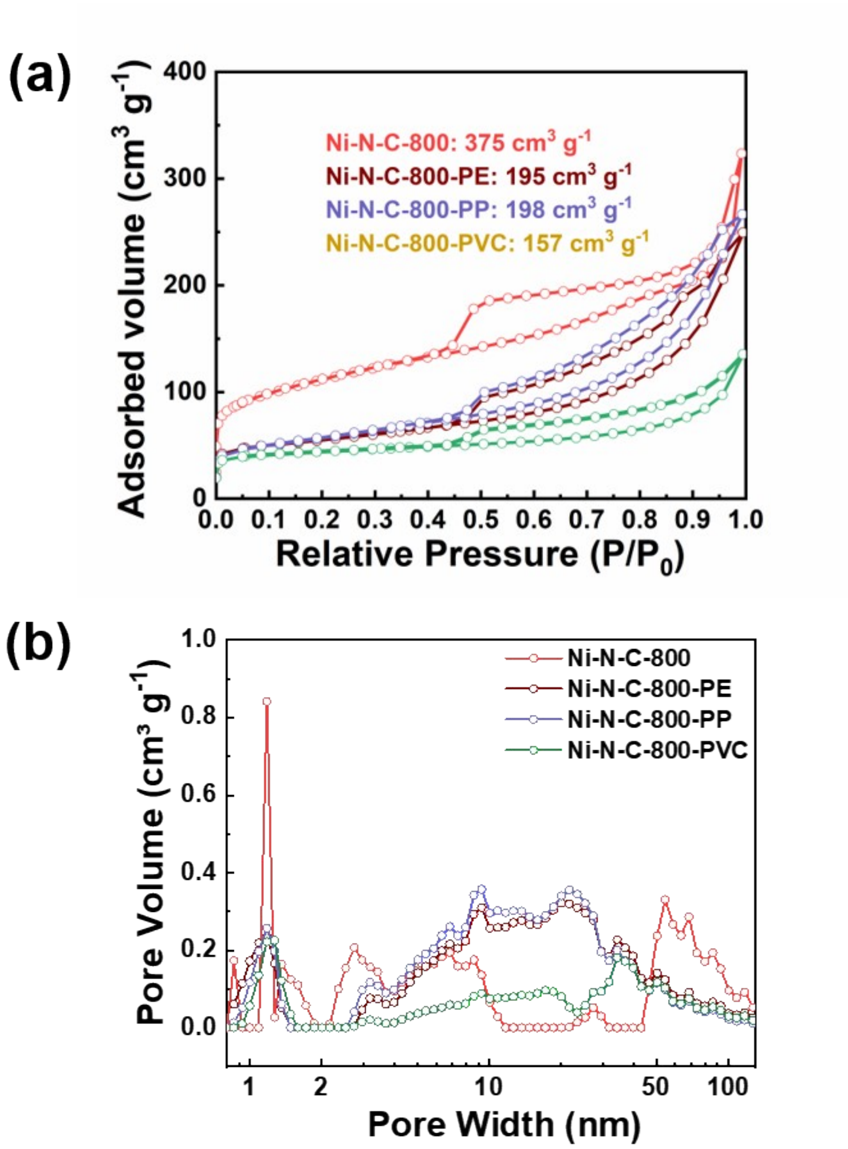

Fig. S20 (a) N_2 adsorption-desorption isotherms and (b) pore size distribution of Ni-N-C-800, Ni-N-C-800-PE, Ni-N-C-800-PP, and Ni-N-C-800-PVC.

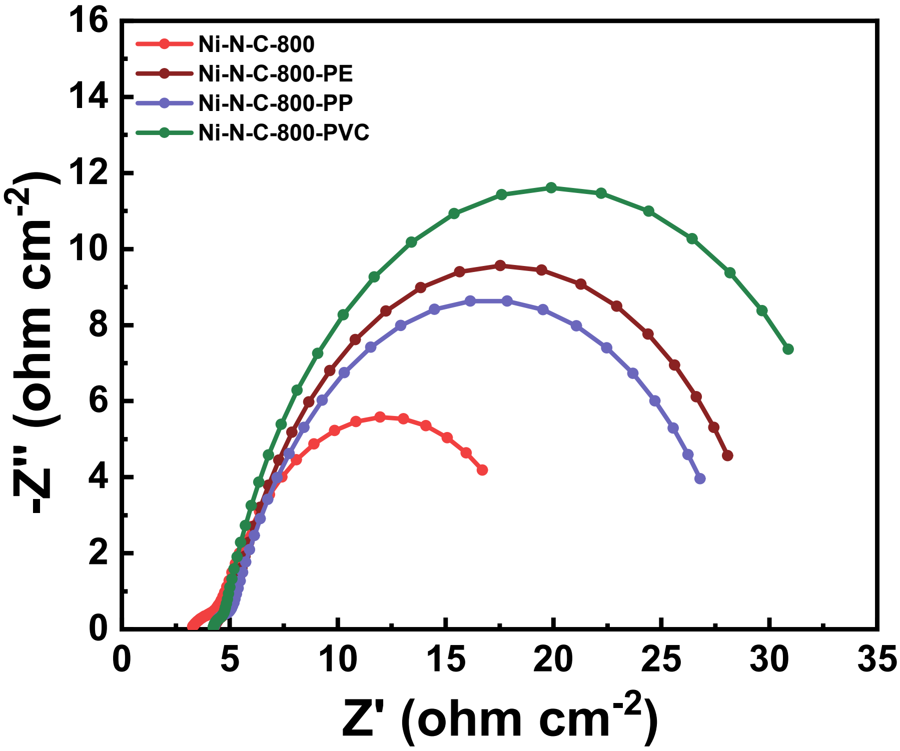

Fig. S21 Nyquist plots of Ni-N-C-800, Ni-N-C-800-PE, Ni-N-C-800-PP, and Ni-N-C-800-PVC.

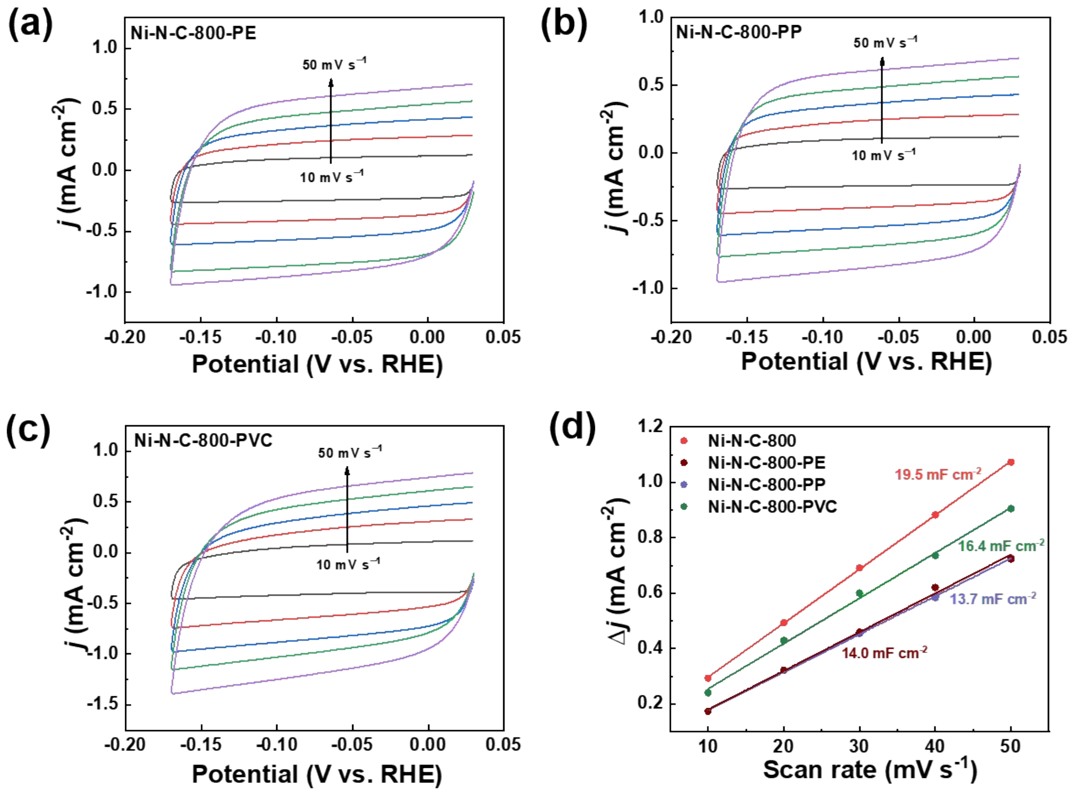

Fig. S22 (a−c) Cyclic voltammograms recorded at Ni-N-C-800-PE, Ni-N-C-800-PP, and Ni-N-C-800-PVC between 0.03 and –0.17 V vs RHE using v = 10, 20, 30, 40 and 50 mV s^{-1} in CO_2-saturated 0.5 M $KHCO_3$; (d) the plot of double layer current density, Δ*j*, obtained at –0.07 V vs RHE from voltammograms (a−c) against the scan rate.

Table S1 The content of C, N, O, and Ni in the Ni-N-C materials determined by XPS and ICP-OES.

Material	C wt% by XPS	N wt% by XPS	O wt% by XPS	Ni wt% by XPS	Ni wt% by ICP-OES
Ni-N-C-700	72.91	13.27	8.27	5.53	3.21
Ni-N-C-800	78.23	9.16	8.02	4.59	2.54
Ni-N-C-900	85.80	3.26	8.75	2.19	1.32
Ni-N-C-800(NS)	79.40	3.60	13.49	3.49	3.81
Ni-C-800	89.77	0.30	9.94	-	0.67
N-C-800	76.29	8.89	14.81	-	-
Ni-N-C-800-PE	83.55	3.36	10.38	2.71	1.65
Ni-N-C-800-PP	84.60	3.54	8.67	3.19	1.90
Ni-N-C-800-PVC	81.24	5.62	9.93	3.22	1.05

Table S2 Impedance information obtained through equivalent circuit fitting.

Material	R_1 (ohm cm^{-2})	R_2 (ohm cm^{-2})	R_3 (ohm cm^{-2})
Ni-N-C-700	3.02	1.29	36.10
Ni-N-C-800	3.16	1.99	19.75
Ni-N-C-900	3.12	1.02	25.35
Ni-N-C-800(NS)	2.80	11.87	62.35
Ni-C-800	3.04	22.50	197.00
N-C-800	3.00	34.13	187.90
Ni-N-C-800-PE	4.27	0.78	25.37
Ni-N-C-800-PP	4.25	0.81	23.88
Ni-N-C-800-PVC	4.23	0.46	30.70

R_1: solution resistance, R_2: ohmic resistance, R_3: charge transfer resistance.

Table S3 BET specific surface areas and pore volumes of materials.

Material	BET surface area（$m^2\ g^{-1}$）	pore volume ($cm^3\ g^{-1}$)
Ni-N-C-700	250	0.206
Ni-N-C-800	375	0.343
Ni-N-C-900	277	0.281
Ni-N-C-800(NS)	282	0.272
Ni-N-C-800-PE	195	0.386
Ni-N-C-800-PP	198	0.412
Ni-N-C-800-PVC	157	0.209

Table S4 EXAFS fitting parameters at the Ni *K*-edge for Ni-N-C-800.

Sample	Shell	CN[a]	*R*(Å)[b]	σ^2 ($Å^2 \cdot 10^{-3}$) [c]	ΔE_0(eV)[d]	*R* factor
Ni-N-C-800	Ni-N	3.93±0.22	1.83±0.04	0.001	10.87±0.95	0.0062

[a]CN, coordination number; [b]*R*, distance between absorber and backscatter atoms; [c]σ^2, Debye-Waller factor to account for both thermal and structural disorders; [d]ΔE_0, inner potential correction; *R* factor indicates the goodness of the fit. Data range for fitting in k-space and *R*-space were 3–11 and 1–2 Å, respectively. *R* factor < 0.02.

Table S5 The performance of Ni-N-C materials for eCO_2RR in flow cells reported in recent years.

Electrocatalyst	Carbon source	Electrolyte	Potential (V vs. RHE)	|*j*| (mA cm^{-2})	FEco (%)	Ref.
N_3NiPc-CNT	CNT	1.0 M KOH	–1.05	250.0	100	[1]
h-Ni/N/C	ZIF-8	1.0 M KOH	–1.3	462.4	93.8	[2]
Ni-N_4/C-NH_2	ZIF-8	1.0 M KOH	–0.9	410	89.3	[3]
NiSA/PCFM	ZIF-8	0.5 M $KHCO_3$	–1.0	308.4	88	[4]
NiSA/NP	CNT	1.0 M KOH	–0.5	346	98	[5]
Ni–N–C-900	ZIF-8	1.0 M KOH	–1.18	726	91	[6]
CBNNiGd-700	Carbon black	1.0 M KOH	–0.91	308	97	[7]
Ni(NC)	Ni-MOF	1.0 M KOH	–1.82	160	99	[8]
Ni-NCB	ZIF-8	0.5 M $KHCO_3$	-	100	100	[9]
InNi DS/NC	ZIF-8	1.0 M KOH	–1.0	317.2	85.2	[10]
Ni-N-C-3	GQDs	1.0 M $KHCO_3$	-	122	95	[11]
Ni@N-C	CNT	1.0 M KOH	–1.07	160	~70	[12]
Ni-PCNF-0.5PMMA	Ni-ZIF-8	1.0 M $KHCO_3$	–1.8	170	94.3	[13]
$(NH_x)_{16}$-NiPc/CNTs	CNT	1.0 M KOH	–1.37	305	100	[14]
Ni-ASCs/4.3 wt.%	Ketjen Black	1.0 M KOH	–1.27	507.2	95.1	[15]
Ni-N-C-800	**PET**	**1.0 M KOH**	**–0.6**	**300**	**99**	**This work**
Ni-N-C-800	**PET**	**1.0 M KOH**	**–1.0**	**400**	**91**	**This work**

References

1 D. D. Ma, S. G. Han, C. S. Cao, W. B. Wei, X. F. Li, B. Chen, X. T. Wu and Q. L. Zhu, Bifunctional single-molecular heterojunction enables completely selective CO_2-to-CO conversion integrated with oxidative 3D nano-polymerization, *Energy Environ. Sci.*, 2021, **14,** 1544-1552.

2 Y. Q. Chen, J. R. Zhang, J. Y. Tian, Y. Guo, F. F. Xu, Y. Zhang, X. Z. Wang, Y. G. Yang, Q. Wu and Z. Hu, Hierarchical Ni/N/C single-site catalyst achieving industrial-level current density and ultra-wide potential plateau of high CO Faradic efficiency for CO_2 electroreduction, *Adv. Funct. Mater.*, 2023, **33,** 2214658.

3 Z. P. Chen, X. X. Zhang, W. Liu, M. Y. Jiao, K. W. Mou, X. P. Zhang and L. C. Liu, Amination strategy to boost the CO_2 electroreduction current density of M-N/C single-atom catalysts to the industrial application level, *Energy Environ. Sci.*, 2021, **14,** 2349-2356.

4 H. P. Yang, Q. Lin, C. Zhang, X. Y. Yu, Z. Cheng, G. D. Li, Q. Hu, X. Z. Ren, Q. L. Zhang, J. H. Liu and C. X. He, Carbon dioxide electroreduction on single-atom nickel decorated carbon membranes with industry compatible current densities, *Nat. Commun.*, 2020, **11,** 593.

5 W. H. Ren, X. Tan, C. Jia, A. Krammer, Q. Sun, J. T. Qu, S. C. Smith, A. Schueler, X. L. Hu and C. Zhao, Electronic regulation of nickel single atoms by confined nickel nanoparticles for energy-efficient CO_2 electroreduction, *Angew. Chem. Int. Ed.*, 2022, **61,** e202203335.

6 Y. Li, N. M. Adli, W. T. Shan, M. Y. Wang, M. J. Zachman, S. Hwang, H. Tabassum, S. Karakalos, Z. X. Feng, G. F. Wang, Y. G. C. Li and G. Wu, Atomically dispersed single Ni site catalysts for high-efficiency CO_2 electroreduction at industrial-level current densities, *Energy Environ. Sci.*, 2022, **15,** 2108-2119.

7 Q. W. Liu, P. Y. Bai, S. L. Wei, C. C. Yang and L. Xu, Gadolinium changes the local electron densities of nickel 3d orbitals for efficient electrocatalytic CO_2 reduction, *Angew. Chem. Int. Ed.*, 2022, **61,** e202201166.

8 C. F. Wen, F. X. Mao, Y. W. Liu, X. Y. Zhang, H. Q. Fu, L. R. Zheng, P. F. Liu and H. G.

Yang, Nitrogen-stabilized low-valent Ni motifs for efficient CO_2 electrocatalysis, *ACS Catal.*, 2019, **10,** 1086-1093.

9 C. M. Zhao, Y. Wang, Z. J. Li, W. X. Chen, Q. Xu, D. S. He, D. S. Xi, Q. H. Zhang, T. W. Yuan, Y. T. Qu, J. Yang, F. Y. Zhou, Z. K. Yang, X. Q. Wang, J. Wang, J. Luo, Y. F. Li, H. H. Duan, Y. Wu and Y. D. Li, Solid-diffusion synthesis of single-atom catalysts directly from bulk metal for efficient CO_2 reduction, *Joule*, 2019, **3,** 584-594.

10 Z. Z. Fan, R. C. Luo, Y. X. Zhang, B. Zhang, P. L. Zhai, Y. T. Zhang, C. Wang, J. F. Gao, W. Zhou, L. C. Sun and J. G. Hou, Oxygen-bridged indium-nickel atomic pair as dual-metal active sites enabling synergistic electrocatalytic CO_2 reduction, *Angew. Chem. Int. Ed.*, 2023, **62,** e202216326.

11 C. Xia, Y. R. Qiu, Y. Xia, P. Zhu, G. H. King, X. Zhang, Z. Y. Wu, J. Y. Kim, D. A. Cullen, D. X. Zheng, P. Li, M. Shakouri, E. Heredia, P. X. Cui, H. N. Alshareef, Y. F. Hu and H. T. Wang, General synthesis of single-atom catalysts with high metal loading using graphene quantum dots, *Nat. Chem.*, 2021, **13,** 887-894.

12 J. Meng, Z. C. Miao, J. Zhang, Z. Wang, R. C. Zhang, L. L. Xu, L. C. Diao, J. Zhou and S. P. Zhuo, One-step synthesis of N-doped carbon nanotubes-encapsulated Ni nanoparticles for efficient electrochemical CO_2 reduction to CO, *J. Alloys Compd.*, 2023, **939,** 168798.

13 H. Wang, H. Y. Chuai, X. Y. Chen, J. L. Lin, S. Zhang and X. B. Ma, Self-supported porous carbon nanofibers decorated with single Ni atoms for efficient CO_2 electroreduction, *ACS Appl. Mater. Interfaces*, 2023, **15,** 1376-1383.

14 S. G. Han, M. Zhang, Z. H. Fu, L. Zheng, D. D. Ma, X. T. Wu and Q. L. Zhu, Enzyme-inspired microenvironment engineering of a single-molecular heterojunction for promoting concerted electrochemical CO_2 reduction, *Adv. Mater.*, 2022, **34,** 2202830.

15 S. G. Wang, Z. Y. Qian, Q. Z. Huang, Y. J. Tan, F. Lv, L. Y. Zeng, C. S. Shang, K. Wang, G. Q. Wang, Y. D. Mao, Y. Wang, Q. H. Zhang, L. Gu and S. J. Guo, Industrial-level CO_2 electroreduction using solid-electrolyte devices enabled by high-loading nickel atomic site catalysts, *Adv. Energy Mater.*, 2022, **12,** 2201278.